THE JOURNAL OF PHYSICAL CHEMISTRY C

Article

Cite This: J. Phys. Chem. C 2019, 123, 16973−16981

pubs.acs.org/JPCC

Superparamagnetic Behavior at Room Temperature through Crystal Chemistry Modification and Particle Assembly Formation: Zinc and Nickel Ferrite Systems

Veronica Blanco-Gutiérrez,*[,†] Adrian Andrada-Chacón,[‡] Javier Sánchez-Benítez,[‡] Esteban Urones-Garrote,[†] Regino Sáez-Puche,[†] and María José Torralvo-Fernández[†]

[†]Departamento Química Inorgánica, Facultad de Ciencias Químicas and [‡]MALTA-Consolider Team, Departamento de Química-Física, Facultad de Ciencias Químicas, Universidad Complutense de Madrid, Ciudad Universitaria, 28040 Madrid, Spain

ABSTRACT: Zinc and nickel ferrites were prepared through a solvothermal method with different microstructures: as assemblies of particles and not forming assemblies. By means of Raman spectroscopy, the cation distribution in the spinel structure has been evaluated for all the samples to understand the magnetic behavior characterization. The influence of the assembly microstructure type into the superparamagnetic behavior has been fully studied, and it seems to drastically increase the magnetic response of the samples through a mechanism of favored dipolar interactions.

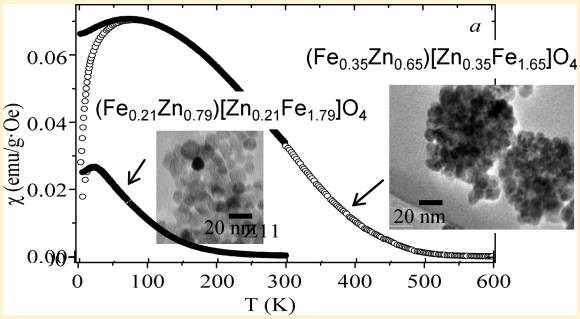

INTRODUCTION

The onset of the nanoscience supposes a milestone in the materials science history.[1,2] Great efforts have been made up to now to investigate the exotic properties of the materials characterized by the so-called finite size effects as a consequence of their nanometric dimensions.[3−7] Superparamagnetism is one of the most studied finite size effects, which consists of illustrating a high magnetic response and noncoercivity under an applied magnetic field.[8−11] This interesting phenomenon is exhibited by magnetic nanoparticles below a critical particle size and for a certain temperature range.[11−13] Consequently, magnetic nanoparticles become one of the most explored materials since they are potential candidates to work with in the field of nanomedicine such as drug delivery agents or for hyperthermia.[14−17] Materials presenting MFe_2O_4 (M = Zn, Ni,...) composition are found to be very convenient candidates for working in such an application field[18,19] due to their chemical stability as well as the use of affordable reagents and soft synthesis conditions for their preparation.[20,21] However, one of the desirable requirements for magnetic nanoparticles to be useful in the field of nanomedicine is to show superparamagnetic properties at room temperature, which seems to occur only in a few systems. Ferrites MFe_2O_4 crystallize with a spinel-type structure (space group, $Fd\bar{3}m$) in which the O^{2-} ions are arranged in a cubic close-packing being one-eighth of tetrahedral (A) and one-half of octahedral (B) sites occupied. While $ZnFe_2O_4$ prepared in the micrometric range presents a cation distribution corresponding to the normal spinel in which the Zn^{2+} cations are located in tetrahedral sites, the cation distribution in $NiFe_2O_4$ with the same microstructural characteristics corresponds to the inverse spinel in which the Ni^{2+} cations occupy octahedral sites. However, when both zinc and nickel ferrites are synthesized in the nanometric range, they present a mixed spinel structure[22−24] $(M_{1-x}Fe_x)[Fe_{2-x}M_x]O_4$ $(0 < x < 1)$, where x is the so-called inversion degree that indicates the cation distribution in the spinel structure. As it is well known, the net magnetization of the ferrite material depends on the compensation of the different sublattices composed by parallel magnetic moments of the atoms. Therefore, the inversion degree fully determines the magnetization of the ferrite compound and is considered as an important parameter to characterize the magnetic behavior of the material. Several techniques such as Mössbauer spectroscopy, neutron diffraction, or synchrotron X-ray absorption spectroscopy are adequate tools to evaluate this parameter.[22,25,26] Moreover, Raman spectroscopy has been recently found to be a very useful nondestructive technique for such a purpose since it is very sensitive to structural disorder.[27]

In the case of single-domain nanoparticles with spinel structures, the magnitude of the magnetic response is directly associated with both the inversion degree and the particle size, which leads to an increment in the coupled moment carriers when it increases.[26] However, it should be underlined that the magnetic behavior of these nanoparticles is drastically influenced by two kinds of interparticle interactions: those occurring between surface spins of different particles and observed at low temperature values and those known as dipole interactions that take place between the magnetic moments of the core of different particles in the superparamagnetic

Received: February 27, 2019
Revised: June 3, 2019
Published: June 12, 2019

DOI: 10.1021/acs.jpcc.9b01898
J. Phys. Chem. C 2019, 123, 16973−16981

temperature range.[28,29] It has been recently observed that some external factors such as temperature, applied magnetic field,[25,30] or the surrounding media of the particles can modify these interactions, thus influencing the superparamagnetic behavior of the material. In this sense, several reports pointed out a drastic influence of the surrounding medium on the superparamagnetic behavior of ferrites. For example, nanoparticles embedded in the amorphous silica behave magnetically harder as a consequence of the stress imposed by the matrix,[31] and porous structures such as sepiolite or faujasite seem to favor the free rotation of the magnetic moment.[32]

To analyze if the microstructure also exerts an important role in the superparamagnetic behavior, both $ZnFe_2O_4$ and $NiFe_2O_4$ have been prepared with two different microstructure types: nonassembled particles and forming assemblies. With the help of Raman spectroscopy, a comparison between the magnetic behaviors corresponding to each microstructural type has been established for the first time, and a detailed evaluation of the crystal chemistry of the samples carried out through Raman spectroscopy is also reported.

EXPERIMENTAL SECTION

The solvothermal method has been used to obtain $ZnFe_2O_4$ and $NiFe_2O_4$ materials as nanosized particles (Z11 and N6 samples, respectively) and particles forming assemblies (ZA11 and NA5 samples, respectively). The number included in the label of the samples refers to the particle size estimated from the TEM images.

Synthesis of Nonassembled Particles. Stoichiometric amounts of iron and zinc or nickel nitrates were dissolved in ethylene glycol to form a 0.01 M solution (typically, 40 mL). The corresponding hydroxides were precipitated with 0.5 and 2.0 M KOH for the Z11 and N6 samples, respectively until reaching pH = 11. Afterward, the obtained brown mixture was transferred into a stainless steel autoclave to be solvothermally treated at 160 °C for 24 h in the case of the Z11 sample and 200 °C for 12 h for the N6 sample. The obtained product was recovered after filtering and washing with distilled water and ethanol.[28,31]

Synthesis of Spherical Particle Assemblies. A 0.36 M solution of the stoichiometric mixture of the nitrates in ethylene glycol was prepared for both ZA11 and NA5 samples (typically, 40 mL). Afterward, sodium acetate trihydrate was added in a 1:1 cations:acetate molar ratio. After stirring for 30 min at room temperature, the mixture was transferred into a Teflon stainless steel autoclave to be solvothermally treated at 200 °C for 4 h (both samples).[33]

The mean particle size estimated after measuring around 100 particles in the TEM images is included (in nanometers) in the label of the four samples. In the same way, "A" included in the labels refers to "assemblies".

Characterization Techniques. The structural characterization was carried out by X-ray diffraction using an X'Pert powder diffractometer (40 mA, 45 kV) with Cu Kα radiation and a 2θ step of 0.02°. Morphological characterization was performed by using transmission electron microscopy (TEM) employing a JEOL-JEM-2100 microscope working at 200 kV and equipped with an XEDS (energy-dispersive X-ray spectroscopy) detector for the compositional analysis.

Raman spectra were collected on a backscattering confocal micro-Raman spectrometer (VoyageTM BWS435-532SY, BW&Tek) equipped with a CCD detector. The excitation was a 532 nm line from a solid-state laser, collected on the sample through a microscope with a 50× objective. The laser power was limited to 2 mW to avoid sample degradation, and the spectral resolution was about 4 cm^{-1}.

The magnetic measurements were obtained using a Quantum Design XL-SQUID magnetometer. Magnetic susceptibility (zero-field cooled (ZFC), field-cooled (FC)) was measured in the temperature range of 2−600 K under a magnetic field of 500 Oe, and magnetization curves were recorded at 5 and 250 K up to a 5 T magnetic field.

RESULTS

Representative TEM images corresponding to ZA11, Z11, NA5, and N6 samples can be observed in Figure 1. While the

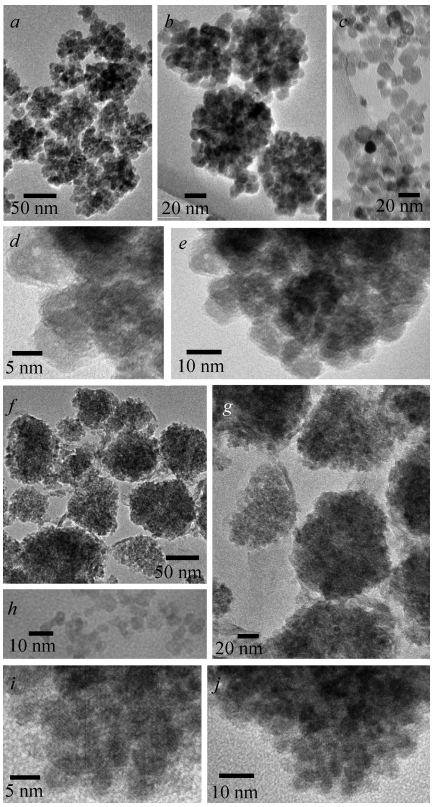

Figure 1. TEM images corresponding to (a, b, d, e) ZA11, (c) Z11, (f, g, i, j) NA5, and (h) N6 samples.

ZA11 sample is composed of spherical assemblies of around 60 nm (Figure 1a,b), in the case of nickel composition, a mean size of 80 nm has been observed for this kind of microstructure (Figure 1f,g). Moreover, different sizes of the particles forming the assemblies have been found depending on the composition; 11 and 5 nm for the ZA11 and NA5 samples, respectively (see Figure 1d,e and Figure 1i,j, respectively). Images shown in Figure 1 for all the samples reveal that the employed solvothermal method allows obtaining particles with homogeneous rounded polyhedral microstructure in the four cases. Moreover, the employment of sodium acetate trihydrate as the precipitant agent effectively leads to a particle assembly microstructure type. HRTEM images are shown in Figure 2 for ZA11 and NA5 samples (Figure 2a,b, respectively), and the 220 interplanar spacing is well identified for both of them (indicated by arrows). It is worth mentioning that for both cases, a continuity of the crystal planes among the particles, which results in large crystal domains (selected areas in the

DOI: 10.1021/acs.jpcc.9b01898
J. Phys. Chem. C 2019, 123, 16973−16981

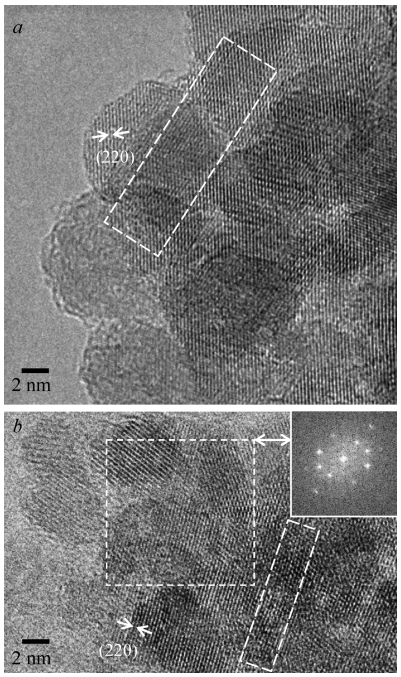

Figure 2. HRTEM images of (a) ZA11 and (b) NA5 samples. Fast Fourier transform of the selected area is shown in the inset of (b) for the NA5 sample.

images with dashed lines), is observed. The fast Fourier transform of the selected area shown for the NA5 sample as an illustration (Figure 2b) confirms the restricted orientation of the planes leading to the observed continuity of the crystal planes among the particles.

Figure 3 illustrates the X-ray diffraction patterns obtained for the different ferrite samples. The diffraction maxima can be

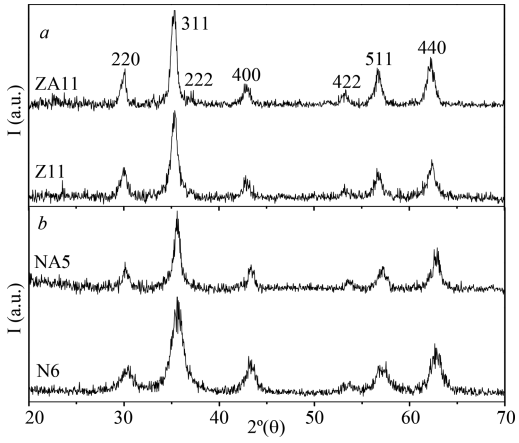

Figure 3. X-ray diffraction patterns corresponding to (a) $ZnFe_2O_4$ and (b) $NiFe_2O_4$ samples.

assigned to crystal planes corresponding to the spinel structure (space group, $Fd\bar{3}m$) (see *hkl* indexes in Figure 3a). It is well known that the intensity ratio between the 220 and 400 reflection maxima gives an idea about the distribution of the M^{2+} and Fe^{3+} cations along the octahedral and tetrahedral sites of the spinel structure.[22,34] Therefore, zinc ferrite samples illustrating a higher ratio (compare diagrams of Figure 3a with those of Figure 3b) may present a crystal structure closer to the normal spinel than nickel ferrite samples. The very broad diffraction maxima reveal the nanometric dimensions of the particles in all the cases. In this sense, crystal domain sizes (D) have been calculated for the four samples through the Scherrer equation[35]

$$D = \frac{0.9\lambda}{\beta \cos \theta} \quad (1)$$

where λ is the Cu Kα radiation (0.154056 nm), and β is the full width at half-maximum of the 311 reflection maximum located at 2θ (around 36°). The values of 10.4 and 10.7 nm have been obtained for Z11 and ZA11 samples, respectively, in good agreement with those sizes estimated from the TEM images. The same occurs for the N6 sample for which a D value of 5.6 nm has been obtained. However, a crystal domain size of 9.5 nm has been calculated from eq 1 for the NA5 sample, which is larger than the particle size estimated from the TEM images. This is in agreement with the crystal coherence observed among the particles in the HRTEM images of Figure 2 that results in larger crystal domains. In the case of the ZA11 sample, the smallest crystal domain size matches up with the mean particle size estimated from the TEM images, while in the case of the NA5 sample, the former one doubles the latter. This indicates that the smallest crystal domain is composed at least of two particles in the NA5 sample, while some of the particles are themselves one single crystal domain in the ZA11 sample. Also, the thicker amorphous surface observable in the ZA11 sample (see Figure 2a) may help to justify the crystal domain size determined by X-ray diffraction.

The Raman spectra of the ferrites samples are shown in Figure 4. The factor group analysis of the cubic spinel structure reveals five Raman-active phonons with symmetries A_{1g}, E_g, and T_{2g}. The A_{1g} phonon is associated to the symmetric stretching of metal−oxygen bonds at the tetrahedral site. The E_g mode corresponds to the symmetric bending of the metal−oxygen bonds at the octahedral sites. Finally, there are three T_{2g} modes, which are due to the asymmetric bending and stretching vibrations at the octahedral sites (T_{2g} (3) and T_{2g} (2), respectively) as well as the translation movement of the whole MO_4 tetrahedral units (T_{2g} (1)). As shown in Table 1, we have assigned the Raman modes according to the symmetry prediction based on factor group analysis and the frequencies previously reported for similar ferrites, finding a good agreement between our results and the literature ones.[20,27,36−39]

The Raman results have been analyzed carrying out a deconvolution of the obtained data by fitting to Lorentzian contributions. We have identified in the spectra a few more modes other than the five active expected phonons. This fact is essentially due to two different reasons. First, some modes usually show a certain splitting that can be ascribed to the mixed character of the spinel. In fact, this phenomenon is drawn on to estimate the inversion degree from the splitting in the A_{1g} mode.[27,36] On the other hand, the presence of additional Raman phonons can be also justified as a consequence of the breakdown of the momentum conservation rule when the particle size (around 5−10 nm in our case) is much smaller than the wavelength of the exciting radiation (532 nm).[37]

By considering the abovementioned, we have estimated the cation disorder in the spinel structure by analyzing the A_{1g} splitting into two components, thus considering the intensity ratio between these two contributions as a direct correlation to the cation distribution in the tetrahedral site.[27,36,39] Similar to

DOI: 10.1021/acs.jpcc.9b01898
J. Phys. Chem. C 2019, 123, 16973−16981

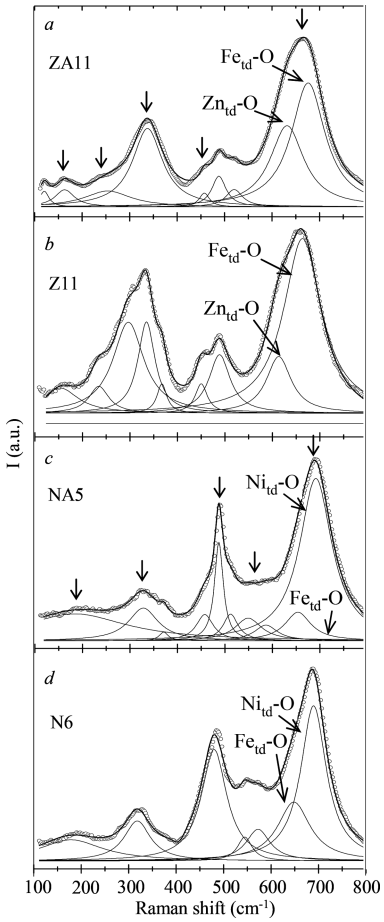

Figure 4. (a–d) Raman spectra for the studied samples. Vertical arrows indicate the position of the five Raman actives modes. Circles represent the experimental data. The thick straight line indicates the obtained convolution from the Lorentzian contributions (thin straight lines). The two A_{1g} contributions for M^{2+} and Fe^{3+} in tetrahedral sites (600–800 nm) are also indicated for the four samples.

the method followed from the previous work in ref 39, the assignment of each A_{1g} contribution to the correct M–O bond (M^{2+}–O and Fe^{3+}–O) was made by comparing the ratio of vibration frequencies ν_{Zn-O}/ν_{Fe-O} or ν_{Ni-O}/ν_{Fe-O} with the bond strength, which are basically conditioned by the bond length. The inversion degree, x, which reflects the M^{2+} content in the tetrahedral sites for the inverse spinel, was estimated through the following equation

$$x(M^{2+}) = \frac{RI_{M^{2+}}}{RI_{M^{2+}} + I_{Fe^{3+}}} \quad (2)$$

where $I_{M^{2+}}$ and $I_{Fe^{3+}}$ are the areas of the A_{1g} contributions, associated with the (M^{2+}–O) and (Fe^{3+}–O) bonds, respectively. From previous experimental works, the parameter R could be considered as 0.5. As a result, we show in Table 1 the estimated values for the inversion degree parameter, x, together with the corresponding mixed spinel formula. It should be noted that similar x values for both nickel ferrite samples are observed, while in the case of the zinc ferrite composition, there is a large difference between both samples (0.35 and 0.21 for ZA11 and Z11 samples, respectively). This reveals the sensitivity of the crystal chemistry of the zinc ferrite system to the synthesis conditions. It is worth mentioning that the estimated inversion degree value for the Z11 sample is in good agreement with that previously calculated by means of neutron diffraction experiment.[23] For nickel ferrite samples, the observed x values are in accordance with those obtained previously by means of Mössbauer and XAS spectroscopies for particles with similar sizes.

Different magnetic parameters, collected in Table 2, have been obtained after certain analyses as explained below.

$M-H$ curves measured at 5 and 250 K are depicted for all the samples in Figure 5. To calculate the magnetization to saturation (M_S) and the effective anisotropy constant (K), the data appearing in the high applied magnetic field region of the $M-H$ curves measured at 5 K have been fitted to the approach to saturation law for each sample[40,41]

$$M(T) = M_S\left(1 - \frac{a}{\sqrt{H}} - \frac{b}{H^2}\right) + cH \quad b = \frac{8}{105}\frac{K^2}{M_S{}^2} \quad (3)$$

where a is a constant, and c corresponds to the magnetic susceptibility in the high applied magnetic field region. The obtained values are collected in Table 2, together with those corresponding to the anisotropy field (H_K) that reflects the intrinsic magnetic hardness of the material. In the case of crystals with cubic symmetry, this magnitude can be obtained from 4[42]

$$H_K = \frac{2K}{M_S} \quad (4)$$

The magnetization to saturation (M_S) at 5 K corresponds to the inherent magnetization of the particles in the blocked state, which is the result of two factors: (1) the net magnetization coming from the compensation of the internal magnetic sublattices and (2) the nonmagnetic surface layer of the particle composed by canted spins. In the case of the zinc ferrite composition, despite the similar particle size for both samples, a higher M_S value is observed for particles forming assemblies (compare the M_S values in Table 2 for ZA11 and Z11 samples), which can be understood taking into account its higher inversion degree (0.35 and 0.21 for ZA11 and Z11, respectively, Table 1). In this sense, the cation distribution $(Zn_{1-x}\overrightarrow{Fe_x})[\overrightarrow{Fe_1}\ \overleftarrow{Fe_{1-x}}Zn_x]O_4$ corresponding to such estimated inversion degrees leads to theoretical M_S values of 81.1 and 48.6 emu/g for ZA11 and Z11, respectively. In the case of the ZA11 sample, the calculated M_S value (81.1 emu/g)

Table 1. Raman Modes and Cation Distribution Corresponding to the Ferrite Samples

	Raman shift (cm^{-1})						
sample	A_{1g}	T_{2g} (3)	T_{2g} (2)	E_g	T_{2g} (1)	x	mixed spinel formula
ZA11	676	457	337	254	163	0.35	$(Fe_{0.35}Zn_{0.65})[Zn_{0.35}Fe_{1.65}]O_4$
Z11	666	453	370	237	155	0.21	$(Fe_{0.21}Zn_{0.79})[Zn_{0.21}Fe_{1.79}]O_4$
NA5	693	567	489	330	185	0.83	$(Fe_{0.83}Ni_{0.17})[Ni_{0.83}Fe_{1.17}]O_4$
N6	691	556	488	320	186	0.79	$(Fe_{0.79}Ni_{0.21})[Ni_{0.79}Fe_{1.21}]O_4$

DOI: 10.1021/acs.jpcc.9b01898
J. Phys. Chem. C 2019, 123, 16973–16981

Table 2. Magnetic Parameters Corresponding to the Ferrite Samples

sample	inversion degree (x)	M_S (emu/g)	K (erg/cm^3)	H_K (Oe)	$H_{C,5}$ (Oe)	T_B (K)	V_{mag} (nm^3)	N_{part}
ZA11	0.35	77.2	3.6·× 10^5	1756	270	79	1480	2
Z11	0.21	40.4	2.3·× 10^5	2144	220	22	561	0.8
NA5	0.83	65.1	2.1·× 10^5	1200	170	144	6955	124
N6	0.79	66.6	1.7·× 10^5	950	224	34	3303	29

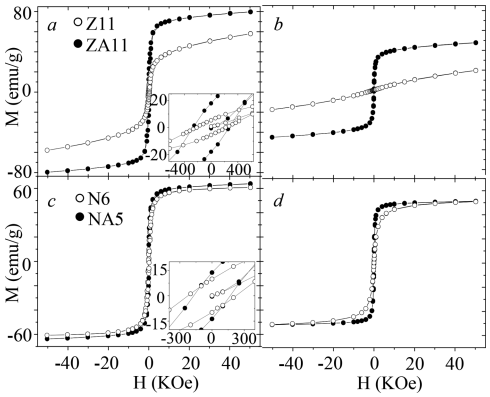

Figure 5. Magnetization curves for the different samples measured at (a, c) 5 K and (b, d) 250 K.

agrees well with the experimental one (77.2 emu/g). The slightly lower experimental M_S value for the Z11 sample (40.4 vs 48.6 emu/g) may be justified considering a nonmagnetic surface layer composed of canted spins that reduces the total magnetization of the sample. The paramagnetic contribution observed in the high applied magnetic field region (increasing magnetization values in the $M-H$ curve measured at 5 K, Figure 5a), which seems to be less important for the ZA11 sample, would be indicative of the presence of this nonmagnetic surface. For the nickel ferrite composition, the similar x value estimated from the Raman spectra would justify the similar M_S values for both samples. Moreover, those values are close to the theoretical M_S ones corresponding to the $(\overrightarrow{Ni}_{1-x}\overrightarrow{Fe}_x)[\overleftarrow{Fe}_{2-x}\overleftarrow{Ni}_x]O_4$ cation distribution estimated from Raman spectroscopy.[22] In the same line, the higher inversion degree observed in the ZA11 sample in comparison with that in Z11 may be responsible for an increment in the magnetocrystalline anisotropy component, thus increasing the effective anisotropy constant and therefore justifying the K value calculated from eq 3 (Table 2) for the ZA11 sample. The corresponding K and M_S values lead to a higher H_K value (see eq 4) for the Z11 sample in comparison with that for the ZA11 one (1756 and 2148 Oe, respectively), which evidences that ferrite particles of the Z11 sample present a higher magnetic hardness, although its effective anisotropy constant is lower. In this sense, it is worth noting the low H_K value of the ZA11 sample, despite its high inversion degree that results in a higher effective anisotropy constant in comparison with the Z11 sample. This can be understood taking into account the presumably more intense dipolar interaction in the case of the ferrite particles forming assemblies (ZA11 sample, see below) that lead to the softening of the magnetic hardness of the material (lower H_K value), which is a lower ($2K/M_S$) ratio (see eq 4).[28] In the case of the nickel ferrite composition, the effective anisotropy constant for NA5 is slightly larger than that for N6, which can be explained taking into account the so similar M_S value but slightly lower particle size (increment in the anisotropy surface component) and higher inversion degree (increment in the magnetocrystalline component) for the NA5 sample. This is also reflected in the H_K parameter, which is larger for the NA5 sample (see eq 4).

Coercive field values at 5 K have been extracted from the $M-H$ curves measured at that temperature (see collected values in Table 2). This parameter can be also described by the following expression[42]

$$H_C = 0.48H_K\left[\left(1 - \frac{T}{T_B}\right)\right]^a \quad (5)$$

where a is a parameter dependent on the interparticle interactions ($0.5 < a < 1$). As the equation indicates, H_C is directly related with H_K, and this dependency is affected by two factors: the blocking temperature, the smaller it is, the more it affects this dependency, and the particle interactions, which affect the a parameter. The higher T_B value of the ZA11 sample (Table 2, explained below), together with a different kind of interparticle interactions influencing the a parameter and lower H_K parameter, would explain its higher H_C value in comparison with Z11 (see eq 5). The very different T_B values observed for the nickel ferrite samples, together with a presuming different a value, would be also responsible for the different coercive fields exhibited at 5 K.

As observed in Figure 5b,d, at 250 K, all the samples illustrate the characteristic S-shape curve, revealing a superparamagnetic behavior, except for the Z11 sample whose $M-H$ curve has a large paramagnetic contribution displaying an almost lineal dependency with very low magnetization values. The already discussed higher inversion degree of the ZA11 sample results in a larger number of superexchange interactions between iron atoms located in octahedral and tetrahedral sites (Fe_B-O-Fe_A), which are characterized by the high values of J_{AB} in comparison with those corresponding to Fe_B-O-Fe_B interactions (J_{BB}). The strength of the Fe_B-O-Fe_A interactions leads to a higher ordering temperature, that is, the internal magnetic ordering of the particle is preserved up to higher temperatures. Thus, ZA11 still behaves as superparamagnetic at 250 K. Through modification of the crystal chemistry of the zinc ferrite sample by using different synthesis conditions, we managed to prepare $ZnFe_2O_4$ particles exhibiting unusual superparamagnetic properties close to room temperature, which makes them more interesting from the point of view of exploitable uses.

The ZFC and FC susceptibility curves measured at 500 Oe have been depicted in Figure 6 for all the samples. The broad ZFC maximum that can be observed for all the samples in comparison with that exhibited by the Z11 sample reveals important dipolar interactions in these cases.[28,43,44] The more intense magnetic responses observed for ZA11 and NA5 samples (see susceptibility curves) can be justified by their higher inversion degrees that increase the magnetic response due to the increment in the number of coupled moment carriers. It should be pointed out that magnetic susceptibility in the superparamagnetic regime decreases with the increment in

DOI: 10.1021/acs.jpcc.9b01898
J. Phys. Chem. C 2019, 123, 16973−16981

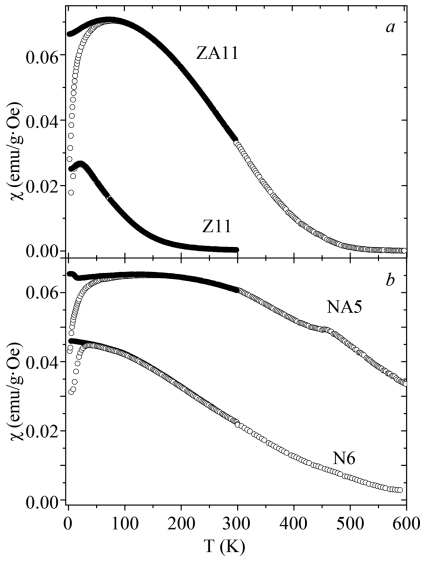

Figure 6. Magnetic susceptibility curves (ZFC, open circle; FC, filled circle) measured at 500 Oe corresponding to the different samples.

the temperature in the case of nonassembled particles and especially in the Z11 sample, and when it comes to particle assemblies, the decrease of the magnetic response is slowed down with the temperature. Due to the particle assembly formation in which dipolar interactions are presumed to be favored, the thermal energy does not easily destroy the magnetic ordering among the particles, and the cooperative phenomenon, resulting in a high magnetic response, is better preserved with the temperature.

It is worth mentioning the observed decreasing trend of the FC curve from T_B to lower temperature values in the case of the zinc ferrite composition. This indicates that for both ZA11 and Z11 samples, the surface spin interactions, occurring at low temperatures, are far from being negligible. When decreasing the temperature from T_B with a 500 Oe applied magnetic field, only an increasing magnetic response is observed in the absence of this kind of interactions as a result of the magnetic−thermal energies balance. On the contrary, in a system with important surface spin interactions, the orientations of the particle dipoles along the direction of the applied field are not allowed at low temperatures, and a decrease in the magnetic response is observed. In this line, the more intense the dipolar interactions are, the less visualized this kind of phenomenon is,[45] evidencing the intensity of this phenomenon when it comes to nickel ferrite samples.

The blocking temperature value has been extracted from the ZFC maximum for all the samples (values collected in Table 2). As it is well known, this parameter depends on the anisotropy barrier (U), and for interacting particles, in the presence of an applied magnetic field, it can be described as follows[46]

$$T_B = \frac{U}{25\kappa_B} \text{ where } U = KV\left(1 - \frac{H}{H_K}\right)^2 \quad (6)$$

where κ_B is the Boltzmann constant, H is the applied magnetic field, and V is the effective magnetic volume usually larger than that observed by TEM (explained below). An increment in the T_B parameter is therefore expected with the increment in the anisotropy barrier. Taking into account the lower values of the effective anisotropy constant and H_K that nickel ferrite samples present, their higher T_B values (see Table 2) may indicate a larger effective magnetic volume (V) in comparison with zinc ferrite samples as eq 6 reveals.[28] Therefore, as previously deduced from the ZFC curve shape, an important number of interacting particles contribute to the total magnetization in the case of nickel ferrite samples. Moreover, the higher T_B values observed in particles forming assemblies in comparison with nonassembled particles reveal more important dipolar interactions for these cases. However, in the case of the ZA11 sample, the higher inversion degree surely contributes to increase this parameter as a consequence of the increment in the effective anisotropy constant.

The effective magnetic volume (V_{mag}) has been calculated from eq 6 for the four samples, taking into account the magnetic parameters collected in Table 2. They are also shown in Table 2. In a rough estimation and considering a spherical particle morphology, almost one and two particles interact in Z11 and ZA11 samples, respectively, (see N_{part} parameter in Table 2), which indicates that not all the particles forming the assemblies for this composition contribute to the effective magnetic volume.[28] On the contrary, around 124 and 29 interacting particles have been found for NA5 and N6 samples, respectively. These qualitative values highlight once again the importance of the dipolar interactions in the nickel ferrite system.

For this kind of samples that present a homogeneous size (see the TEM images of Figure 1), an easy way to visualize the effective magnetic volume distribution with the temperature is through the $-d(\chi_{FC} - \chi_{ZFC})/dT$ curves[28] since the maximum of the curve is directly related with the anisotropy barriers distribution (KV) (see curves depicted in Figure 7 for all the

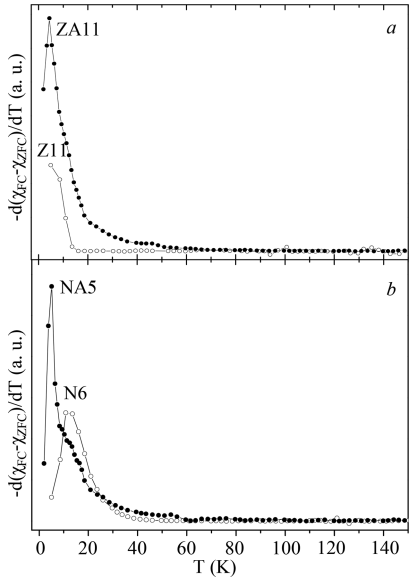

Figure 7. $-d(\chi_{FC} - \chi_{ZFC})/dT$ curves corresponding to the (a) $ZnFe_2O_4$ and (b) $NiFe_2O_4$ samples.

samples). In the case of the Z11 sample, a narrow maximum can be presumed in comparison with the rest of the samples (Figure 7a). The narrower anisotropy barrier observed for this case can be directly related with a narrow distribution of the effective magnetic volume. On the contrary, for the rest of the samples, a progressively number of interacting particles

DOI: 10.1021/acs.jpcc.9b01898
J. Phys. Chem. C 2019, 123, 16973−16981

contributing to the magnetization (increasing effective magnetic volume) widen the distribution of the effective magnetic volume, thus enlarging the observed maxima shown in Figure 7. Moreover, it should be pointed out that the minimum illustrated by the curves at temperature values corresponding to the T_B indicates that all the anisotropy barriers have been overcome for such temperatures, thus regarding all the particles as superparamagnetic.

Several works reported on the effect of the dipolar interactions in the total magnetization of the samples.[28,29,47] As consequence of a dependence of the interparticle interactions with temperature, the effective superparamagnetic moment (μ_{SP}) also presents an evolution with T, and it can be calculated through the following expression[45]

$$\mu_{SP}(\mu_B)(T) = \frac{3\kappa_B}{M_S\mu_B}\left[\frac{d(1/\chi)}{dT}\right]^{-1} \quad (7)$$

The obtained curves are represented in Figure 8 for all the samples. The maximum observed for all of them indicates the temperature for which the dipolar interactions responsible for the cooperative phenomenon are more intense, leading to higher superparamagnetic moment. In all the cases, this maximum seems to be close to the T_B since it corresponds to the temperature for which all the anisotropy barriers have been totally overcome, thus contributing most of the particles to the magnetization.

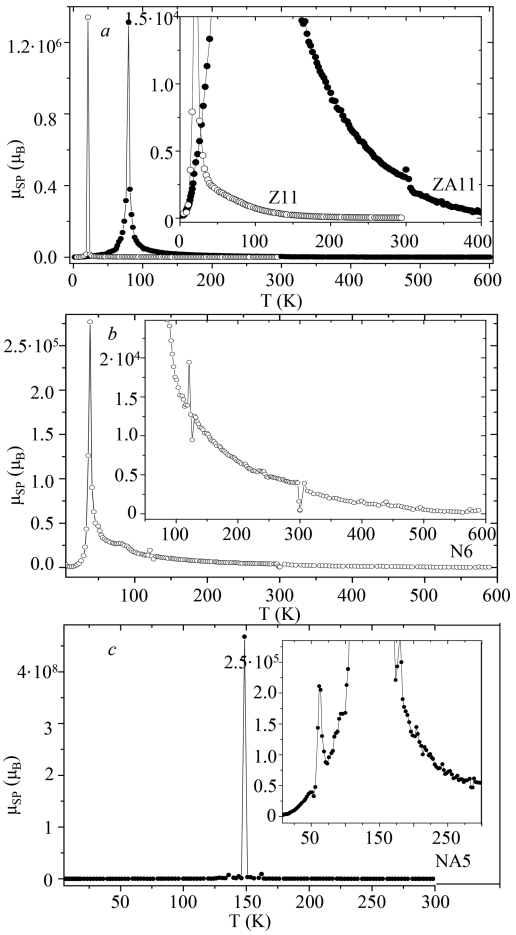

Figure 8. Superparamagnetic moment dependence with the temperature for (a) Z11 and ZA11, (b) N6, and (c) NA5 samples.

The μ_{SP} magnitude for a certain temperature is the result of two contributing factors: the net magnetization per particle and the number of interacting particles. Taking this into consideration, although the highest μ_{SP} presents a similar value when it comes to zinc ferrite samples, the maximum is much broader in the case of the particles forming assemblies, indicating that the cooperative phenomenon is extended in the temperature range. As it can be observed in the inset of Figure 8a, much higher μ_{SP} values are observed for the ZA11 sample along the temperature range (roughly from 20 to 150 K), revealing that the responsible dipolar interactions are better preserved with the temperature, while in the case of the Z11 sample, the relatively high magnetic response is only observable in a very narrow temperature range (from 15 to 25 K approximately). In general, curves corresponding to nickel ferrite samples illustrate higher superparamagnetic values than in the case of zinc ferrite composition (Figure 8). This fact is in agreement with their larger intrinsic magnetization and more intense dipolar interactions (see V_{mag} and N_{part} values in Table 2).

Interesting results concerning the magnitude of the superparamagnetic moment has been found for both ferrite compositions. At 300 K, nonassembled zinc ferrite particles illustrate a superparamagnetic moment value (see eq 7) around 200 μ_B, while those particles forming assemblies present an μ_{SP} close to 3000 μ_B, which supposes 1 order of magnitude higher magnetic response (Figure 8a). In the case of zinc ferrite samples, crystal chemistry plays an important role in determining the inherent magnetic moment of the particles directly related with the magnetic response of the sample. However, this specific microstructure seems to be a booster for more intense dipolar interactions, which are preserved along the temperature range, thus displaying a high magnetic response in the studied superparamagnetic temperature range. Something similar can be observed in the studied nickel ferrite samples, although for this composition, a high μ_{SP} close to 3500 μ_B (Figure 8b) is already observed in the case of nonassembled particles of 6 nm (in comparison with the very low magnitude corresponding to nonassembled zinc ferrite 11 nm particles). In contrast, the nickel ferrite sample composed of particle assemblies for which the internal magnetic moment is close to that corresponding to nonassembled particles, illustrates 1 order of magnitude higher superparamagnetic moment of around 50,000 μ_B. The influence of the microstructure in the magnetic response of the material is therefore fully demonstrated, and particle assemblies formation results as a useful tool to increase nearly 1 order of magnitude the superparamagnetic response of these materials. As discussed above, the different crystal chemistry found for $ZnFe_2O_4$ particles forming assemblies also contributes in increasing the superparamagnetic response.

CONCLUSIONS

Two kinds of microstructure for zinc ferrite and nickel ferrite particles have been obtained through synthesis condition modification of the solvothermal method. In addition, in the case of zinc ferrite composition, the crystal chemistry is seemingly influenced by the experimental conditions.

Two ways of increasing the superparamagnetic response were established: by modifying the inversion degree in the spinel structure, which leads to a larger inherent magnetization

DOI: 10.1021/acs.jpcc.9b01898
J. Phys. Chem. C 2019, 123, 16973−16981

per particle (larger M_S value), and through the particle assembly formation that seems to be a booster of the dipolar interactions, thus preserving a high magnetic response up to room temperature values. In the case of nickel ferrite samples, their superparamagnetic behavior has been fully ascribed to the role of the microstructure. In this sense, it has been observed that while in the case of nonassembled particles, around 30 particles contribute to the magnetization for a certain temperature close to the T_B, those forming assemblies present an effective magnetic volume corresponding to an estimated value of 124 particles. $ZnFe_2O_4$ samples present an increase in the superparamagnetic response ascribable not only to the assembly microstructure but also to the modification of the inversion degree parameter.

AUTHOR INFORMATION

Corresponding Author

*E-mail: veronicabg@quim.ucm.es.

ORCID

Veronica Blanco-Gutiérrez: 0000-0002-0619-389X

Javier Sánchez-Benítez: 0000-0002-3108-6594

Notes

The authors declare no competing financial interest.

ACKNOWLEDGMENTS

The authors are grateful to the MICINN and MINECO for the financial support under projects MALTA-Consolider (CSD2007-00045, MAT2015-71070-REDC) and CTQ2015-67755-C2-1R (MINECO/FEDER) and to Centro de Microscopia Electronica, CAI de Difraccion de Rayos X, and CAI de Tecnicas Fisicas at Universidad Complutense de Madrid for the technical assistance. A.A.-C. acknowledges the support from a MINECO-FPI grant (BES-2013-066112), and J.S.-B. is also grateful to MINECO for the Ramon y Cajal (RyC-2010-06276) fellowship.

REFERENCES

(1) Chan, W. W. C.; Chhowalla, M.; Glotzer, S.; Gogotsi, Y.; Hafner, J. H.; Hammond, P. T.; Hersam, M. C.; Javey, A.; Kagan, C. R.; Khademhosseini, A.; et al. Nanoscience and Nanotechnology Impacting Diverse Fields of Science, Engineering, and Medicine. *ACS Nano* **2016**, *10*, 10615−10617.

(2) Mulvaney, P.; Weiss, P. S. Have Nanoscience and Nanotechnology Delivered? *ACS Nano* **2016**, *10*, 7225−7226.

(3) Pati, S. P.; Al-Mahdawi, M.; Ye, S.; Shiokawa, Y.; Nozaki, T.; Sahashi, M. Finite-size scaling effect on Néel temperature of antiferromagnetic Cr2O3 (0001) films in exchange-coupled heterostructures. *Phys. Rev. B* **2016**, *94*, 224417.

(4) Silva, J.; Oliveira, M. J. T.; Lanceros-Mendez, S.; Nogueira, F. Finite-Size Effects in the Absorption Spectra of a Single-Wall Carbon Nanotube. *J. Phys. Chem. C* **2016**, *120*, 18268−18274.

(5) Eliseev, E. A.; Kalinin, S. V.; Morozovska, A. N. Finite size effects in ferroelectric-semiconductor thin films under open-circuit electric boundary conditions. *J. Appl. Phys.* **2015**, *117*, No. 034102.

(6) Mikolasek, M.; Félix, G.; Peng, H.; Rat, S.; Terki, F.; Chumakov, A. I.; Salmon, L.; Molnár, G.; Nicolazzi, W.; Bousseksou, A. *Phys. Rev. B* **2017**, *96*, No. 035426.

(7) Blanco-Gutierrez, V.; Demourgues, A.; Gaudon, M. Submicrometric β-CoMoO4 rods: optical and piezochromic properties. *Dalton Trans.* **2013**, *42*, 13622−13627.

(8) Batlle, X.; Labarta, A. Finite-size effects in fine particles:magnetic and transport properties. *J. Phys. D: Appl. Phys.* **2002**, *35*, R15.

(9) Kodama, R. H. Magnetic nanoparticles. *J. Magn. Magn. Mater.* **1999**, *200*, 359−372.

(10) Papaefthymiou, G. C. Nanoparticle magnetism. *Nano Today* **2009**, *4*, 438−447.

(11) Knobel, M.; Nunes, W. C.; Socolovsky, L. M.; De Biasi, E.; Vargas, J. M.; Denardin, J. C. Superparamagnetism and other magnetic features in granular materials: a review on ideal and real systems. *J. Nanosci. Nanotechnol.* **2008**, *8*, 2836−2857.

(12) Mørup, S.; Hansen, M. F.; Frandsen, C. Magnetic Nanoparticles. *Compr. Nanosci. Technol.* **2011**, *1*, 437−491.

(13) Skomski, R. Nanomagnetics. *J. Phys. Condens. Matter.* **2003**, *15*, R841−R896.

(14) Tartaj, P. Nanomagnets-From fundamental physics to biomedicine. *Curr. Nanosci.* **2006**, *2*, 43−53.

(15) Zamora-Mora, V.; Fernández-Gutiérrez, M.; González-Gómez, Á.; Sanz, B.; Román, J. S.; Goya, G. F.; Hernández, R.; Mijangos, C. Chitosan nanoparticles for combined drug delivery and magnetic hyperthermia: From preparation to in vitro studies. *Carbohydr. Polym.* **2017**, *157*, 361−370.

(16) Conde-Leboran, I.; Baldomir, D.; Martinez-Boubeta, C.; Chubykalo-Fesenko, O.; del Puerto Morales, M.; Salas, G.; Cabrera, D.; Camarero, J.; Teran, F. J.; Serantes, D. A Single Picture Explains Diversity of Hyperthermia Response of Magnetic Nanoparticles. *J. Phys. Chem. C* **2015**, *119*, 15698−15706.

(17) Starsich, F. H. L.; Eberhardt, C.; Boss, A.; Hirt, A. M.; Pratsinis, S. E. Coercivity determines Magnetic Particle Heating. *Adv. Health Care Mater.* **2018**, *7*, 1800287.

(18) Castellanos-Rubio, I.; Insausti, M.; Garaio, E.; Gil de Muro, I.; Plazaola, F.; Rojo, T.; Lezama, L. Fe3O4 nanoparticles prepared by the seeded-growth route for hyperthermia: electron magnetic resonance as a key tool to evaluate size distribution in magnetic nanoparticles. *Nanoscale* **2014**, *6*, 7542−7552.

(19) Serantes, D.; Simeonidis, K.; Angelakeris, M.; Chubykalo-Fesenko, O.; Marciello, M.; del Puerto Morales, M.; Baldomir, D.; Martinez-Boubeta, C. Multiplying Magnetic Hyperthermia Response by Nanoparticle Assembling. *J. Phys. Chem. C* **2014**, *118*, 5927−5934.

(20) Pereira, C.; Pereira, A. M.; Fernandes, C.; Rocha, M.; Mendes, R.; Fernández-García, M. P.; Guedes, A.; Tavares, P. B.; Grenèche, J. M.; Araújo, J. P.; et al. Superparamagnetic MFe2O4(M = Fe, Co, Mn) Nanoparticles: Tuning the Particle Size and Magnetic Properties through a Novel One-Step Coprecipitation Route. *Chem. Mater.* **2012**, *24*, 1496−1504.

(21) Grasset, F.; Labhsetwar, N.; Li, D.; Park, D. C.; Saito, N.; Haneda, H.; Cador, O.; Roisnel, T.; Mornet, S.; Duguet, E.; et al. Synthesis and magnetic characterization of zinc ferrite nanoparticles with different environments: Powder, colloidal solution, and zinc ferrite-silica core-shell nanoparticles. *Langmuir* **2002**, *18*, 8209−8216.

(22) Blanco-Gutiérrez, V.; Gallastegui, J. A.; Bonville, P.; Torralvo-Fernández, M. J.; Sáez-Puche, R. MFe2O4 (M: Co2+, Ni2+) Nanoparticles: Mössbauer and X-ray Absorption Spectroscopies Studies and High-Temperature Superparamagnetic Behavior. *J. Phys. Chem. C* **2012**, *116*, 24331−24339.

(23) Blanco-Gutierrez, V.; Climent-Pascual, E.; Torralvo-Fernandez, M. J.; Saez-Puche, R.; Fernandez-Diaz, M. T. Neutron diffraction study and superparamagnetic behavior of ZnFe2O4 nanoparticles obtained with different conditions. *J. Solid State Chem.* **2011**, *184*, 1608−1613.

(24) Šepelák, V.; Bergmann, I.; Feldhoff, A.; Heitjans, P.; Krumeich, F.; Menzel, D.; Litterst, F. J.; Campbell, S. J.; Becker, K. D. Nanocrystalline Nickel Ferrite, NiFe2O4 : Mechanosynthesis , Nonequilibrium Cation Distribution , Canted Spin Arrangement , and Magnetic Behavior. *J. Phys. Chem. C* **2007**, *111*, 5026−5033.

(25) Blanco-Gutiérrez, V.; Climent-Pascual, E.; Sáez-Puche, R.; Torralvo-Fernández, M. J. Temperature dependence of superparamagnetism in CoFe2O4 nanoparticles and CoFe2O4/SiO2 nanocomposites. *Phys. Chem. Chem. Phys.* **2016**, *18*, 9186−9193.

(26) Ngo, A. T.; Bonville, P.; Pileni, M. P. Spin canting and size effects in nanoparticles of nonstoichiometric cobalt ferrite. *J. Appl. Phys.* **2001**, *89*, 3370−3376.

(27) Jovanović, S.; Spreitzer, M.; Tramšek, M.; Trontelj, Z.; Suvorov, D. Effect of Oleic Acid Concentration on the Physicochem-

DOI: 10.1021/acs.jpcc.9b01898
J. Phys. Chem. C 2019, 123, 16973−16981

ical Properties of Cobalt Ferrite Nanoparticles. *J. Phys. Chem. C* **2014**, *118*, 13844−13856.
(28) Blanco-Gutierrez, V.; Saez-Puche, R.; Torralvo-Fernandez, M. J. Superparamagnetism and interparticle interactions in ZnFe2O4 nanocrystals. *J. Mater. Chem.* **2012**, *22*, 2992−3003.
(29) Moya, C.; Iglesias, Ó.; Batlle, X.; Labarta, A. Quantification of Dipolar Interactions in Fe3−xO4 Nanoparticles. *J. Phys. Chem. C* **2015**, *119*, 24142−24148.
(30) Blanco-Gutiérrez, V.; Torralvo-Fernández, M. J.; Sáez-Puche, R. Innovative study of superparamagnetism in 3 nm CoFe2O4particles. *RSC Adv.* **2016**, *6*, 87995−88000.
(31) Blanco-Gutierrez, V.; Virumbrales, M.; Saez-Puche, R.; Torralvo-Fernandez, M. J. Superparamagnetic behavior of MFe2O4 Nanoparticles and MFe2O4/SiO2 Composites (M: Co, Ni). *J. Phys. Chem. C* **2013**, *117*, 20927−20935.
(32) Blanco-Gutiérrez, V.; Urones-Garrote, E.; Torralvo-Fernández, M. J.; Sáez-Puche, R. ZnFe2O4 Nanoparticles: Different magnetic behavior when they are hosted in porous structures. *Chem. Mater.* **2010**, *22*, 6130−6137.
(33) Liu, J.; Zhang, Y.; Nan, Z. Facile synthesis of stoichiometric zinc ferrite nanocrystal clusters with superparamagnetism and high magnetization. *Mater. Res. Bull.* **2014**, *60*, 270−278.
(34) Michel, A. *Phénomènes Magnétiques Et Structure*; Masson et Cie: Paris, **1966**.
(35) Patterson, A. L. The Scherrer Formula for X-Ray Particle Size Determination. *Phys. Rev.* **1939**, *56*, 978−982.
(36) Nakagomi, F.; da Silva, S. W.; Garg, V. K.; Oliveira, A. C.; Morais, P. C.; Franco, A., Jr. Influence of the Mg-content on the cation distribution in cubic MgxFe3-xO4 nanoparticles. *J. Solid State Chem.* **2009**, *182*, 2423−2429.
(37) Jacintho, G. V. M.; Brolo, A. G.; Corio, P.; Suarez, P. A. Z.; Rubim, J. C. Structural Investigation of MFe2O4 (M = Fe, Co) Magnetic Fluids. *J. Phys. Chem. C* **2009**, *113*, 7684−7691.
(38) Lazarević, Z. Z.; Jovalekić, C.; Milutinović, A.; Sekulić, D.; Ivanovski, V. N.; Rečnik, A.; Cekić, B.; Romcević, Z. Nanodimensional spinel NiFe2O4 and ZnFe2O4 ferrites prepared by soft mechanochemical synthesis. *J. Appl. Phys.* **2013**, *113*, 187221.
(39) Virumbrales-del Olmo, M.; Delgado-Cabello, A.; Andrada-Chacón, A.; Sánchez-Benítez, J.; Urones-Garrote, E.; Blanco-Gutiérrez, V.; Torralvo, M. J.; Sáez-Puche, R. Effect of composition and coating on the interparticle interactions and magnetic hardness of MFe2O4(M = Fe, Co, Zn) nanoparticles. *Phys. Chem. Chem. Phys.* **2017**, *19*, 8363−8372.
(40) Mitra, S.; Mandal, K.; Anil Kumar, P. Temperature dependence of magnetic properties of NiFe2O4 nanoparticles embeded in SiO2 matrix. *J. Magn. Magn. Mater.* **2006**, *306*, 254−259.
(41) Jin, Z.-Q.; Tang, W.; Zhang, J.-R.; Qin, H.-X.; Du, Y.-W. Effective magnetic anisotropy of nanocrystalline Nd-Fe-Ti-N hard magnetic alloys. *Eur. Phys. J. B* **1998**, *3*, 41−44.
(42) Gubin, S. P.; Koksharov, Y. A.; Khomutov, G. B.; Yurkov, G. Y. Magnetic nanoparticles: preparation, structure and properties. *Russ. Chem. Rev.* **2005**, *74*, 489−520.
(43) Vestal, C. R.; Zhang, Z. J. Effects of surface coordination chemistry on the magnetic properties of MnFe2O4 Spinel ferrite nanoparticles. *J. Am. Chem. Soc.* **2003**, *125*, 9828−9833.
(44) Sharma, S. K.; Vargas, J. M.; de Biasi, E.; Béron, F.; Knobel, M.; Pirota, K. R.; Meneses, C. T.; Kumar, S.; Lee, C. G.; Pagliuso, P. G.; et al. The nature and enhancement of magnetic surface contribution in model NiO nanoparticles. *Nanotechnology* **2010**, *21*, 035602.
(45) Virumbrales, M.; Sáez-Puche, V.; Blanco-Gutiérrez, V.; Torralvo-Fernández, M. J. Discussion on the Interparticle Interactions in NiFe2O4 and ZnFe2O4 Nanosized Systems Based on the Matrix Effects in the Magnetic Behavior. *J. Phys. Chem. C* **2017**, *121*, 4029−4036.
(46) Zheng, R. K.; Gu, H.; Xu, B.; Zhang, X. X. The origin of the non-monotonic field dependence of the blocking temperature in magnetic nanoparticles. *J. Phys. Condens. Matter* **2006**, *18*, 5905−5910.
(47) Coral, D. F.; Zélis, P. M.; Marciello, M.; del Puerto Morales, M.; Craievich, A.; Sánchez, F. H.; Fernández van Raap, M. B. Effect of Nanoclustering and Dipolar Interactions in Heat Generation for Magnetic Hyperthermia. *Langmuir* **2017**, *32*, 1201−1213.

DOI: 10.1021/acs.jpcc.9b01898
J. Phys. Chem. C 2019, 123, 16973−16981